

Original Research

Comprehensive Multi-Omics Analysis Identifies Lactylation-Related Gene *RAN* as a Novel Prognostic Biomarker and Therapeutic Target in Glioma

Shunda Wang^{1,2,3}, Fan Tang^{1,2,3}, Hong Chen^{1,2,3}, Jingyue Pang^{1,2,3}, Ying Zhang^{1,2,3}, Jianjing Yang^{1,2,3,*} , Yue Zhang^{4,*} 

¹Department of Neurosurgery, The First Affiliated Hospital of Wenzhou Medical University, 325000 Wenzhou, Zhejiang, China

²Zhejiang-US Joint Laboratory for Aging and Neurological Disease Research, The First Affiliated Hospital of Wenzhou Medical University, 325000 Wenzhou, Zhejiang, China

³Zhejiang Provincial Key Laboratory of Aging and Neurological Disorder Research, The First Affiliated Hospital of Wenzhou Medical University, 325000 Wenzhou, Zhejiang, China

⁴Department of Otolaryngology, Wenzhou People's Hospital, 325000 Wenzhou, Zhejiang, China

*Correspondence: yangjianjing@wmu.edu.cn (Jianjing Yang); zy5809@126.com (Yue Zhang)

Academic Editor: Thomas Heinbockel

Submitted: 20 September 2025 Revised: 23 November 2025 Accepted: 28 November 2025 Published: 18 December 2025

Abstract

Background: Gliomas are the most aggressive primary malignancies of the central nervous system (CNS) and exhibit marked heterogeneity that is closely associated with metabolic reprogramming. Emerging evidence underscores the pivotal role of lactylation modifications in shaping the tumor microenvironment (TME) and facilitating glioma progression. This study aimed to systematically identify key lactylation-related genes (LRGs), elucidate their functional roles and associated pathways, and explore their potential as novel therapeutic targets using multi-omics data. **Methods:** We combined various datasets from the TCGA, GEO, and CGGA databases, including RNA-seq, single-cell RNA sequencing (scRNA-seq), and spatial transcriptomics. Key LRGs were identified through a multi-step analytical pipeline that involved processing scRNA-seq data using (Seurat, scoring), cell-type-specific lactylation scoring (AUCell), high-dimensional weighted gene co-expression network analysis (hdWGCNA) and applying rigorous machine learning-based feature selection utilizing 10 algorithms and 101 combinatorial strategies. We comprehensively assessed the prognostic value associated with the immune microenvironment, and spatiotemporal heterogeneity of the prioritized *RAN*. Functional validation was executed using shRNA-mediated knockdown in glioma cell lines, including LN229, U87, and U251, while evaluating proliferation (CCK-8, colony formation, EdU), migration (wound healing), invasion (Transwell), and pathway activity (using western blot). **Results:** scRNA-seq analysis revealed distinct lactylation enrichment patterns across glioma cell types, with malignant cells exhibiting the highest scores. hdWGCNA identified a gene module (royal blue) strongly correlated with lactylation activity (correlation = 0.75). The intersection of this module with a curated set of LRGs yielded 22 candidate genes. Subsequent machine learning analysis using (ENet, $\alpha = 0.4$) prioritized six core LRGs (PDAP1, ALYREF, CBX3, MAGOH, RAN, TMSB4X). *RAN*, an understudied gene in glioma, was selected for further investigation. High *RAN* expression correlated significantly with poor patient prognosis, reduced immune cell infiltration (assessed by ESTIMATE, CIBERSORT, xCell, ssGSEA), and distinct spatiotemporal heterogeneity within tumors (analyzed using spatial transcriptomics, Monocle2). Glioma cell invasion, migration, colony formation, and proliferation were all markedly inhibited by *RAN* knockdown. Mechanistically, reduced p-AKT levels following knockdown and functional rescue with a PI3K/AKT activator (SC79) indicate that *RAN* increased these malignant traits by activating the PI3K/AKT signaling pathway. **Conclusion:** Our study established lactylation modifications as a crucial regulator of the TME and glioma progression. Through integrative multi-omics analysis and robust machine learning techniques, we determined that *RAN* was a novel lactylation-associated gene. *RAN* is a potent, independent prognostic biomarker that promotes glioma malignancy via the PI3K/AKT pathway. Our results demonstrate *RAN* as a prospective therapeutic target and establish a novel framework for individualized therapy for glioma.

Keywords: glioma; lactylation; machine learning; tumor microenvironment

1. Introduction

Gliomas account for the majority of primary malignant tumors in the central nervous system (CNS). The 2021 WHO Classification of Tumors of the CNS (WHO CNS5) categorizes diffuse gliomas into three major types: astrocytomas (WHO grades 2–4), oligodendrogliomas (WHO grades 2–3), and glioblastoma (WHO

grade 4) [1]. Glioblastoma (GBM), the most aggressive subtype, accounts for approximately 48% of primary brain malignancies. Despite standard treatment involving maximal safe resection followed by radiotherapy with concurrent and adjuvant temozolomide (Stupp protocol) [2], the prognosis remains dismal. People with this disease can only live for 12 to 15 months on average, and less than 5% can



live for 5 years. The complex pathogenesis of GBM necessitates the discovery of novel therapeutic targets. Molecular markers play an increasingly vital role in glioma diagnosis, prognostication, and classification. While the WHO CNS5 classification incorporates key molecular alterations (e.g., IDH1/2 mutation, 1p/19q codeletion, CDKN2A/B deletion, EGFR amplification) [3], there remains a pressing need to find additional robust biomarkers to enhance patient stratification and guide the development of targeted therapies.

Lactate, we used to think it was just a glycolytic waste in the body, but now we find it is actually a very important signal molecule. Lactylation is a post-translational modification (PTM), which is characterized by linking the lactyl group from lactic acid to the lysine residues of histone and non-histone protein. In this way, a “metabolic-epigenetic coupling network” has been formed, which has a profound impact on tumor biology [4]. In glioblastoma, lactylation contributes significantly to tumor progression and therapy resistance. For instance, ACSS2/KAT2A-mediated histone H3K14/K18 lactylation activates Wnt/NF- κ B signaling and upregulates PD-L1, fostering an immunosuppressive TME [5]. Lactylation of XRCC1 at K247, driven by the ALDH1A3-PKM2 axis, enhances DNA repair efficiency, conferring radioresistance to glioma stem cells (GSCs) [6]. Furthermore, PTBP1 lactylation at K436 stabilizes PFKFB4 mRNA, creating a positive feedback loop that sustains high glycolytic flux and stemness in GSCs [7]. These results highlight the crucial significance of dissecting the lactylation regulatory network and identifying lactylation-associated gene targets for advancing glioma diagnosis and treatment.

Despite this progress, systematic investigations of lactylation-related genes (LRGs) within the complex glioma TME remain limited. While numerous studies have sought glioma molecular markers, many suffer from reliance on single datasets and lack comprehensive multi-dimensional validation. Moreover, rigorous experimental confirmation of identified targets and their mechanistic pathways is often insufficient.

Herein, we use a comprehensive multi-omics method combining transcriptomics (Bulk and Single-cell), spatial transcriptomics, and sophisticated computational algorithms (Seurat, AUCcell, hdWGCNA, ensemble machine learning) to systematically identify key LRGs driving glioma progression. Through this strategy, we prioritized the *RAN* (Ras-related nuclear protein) gene for further investigation. We comprehensively characterized the association of *RAN* expression with patient prognosis, TME, and spatiotemporal heterogeneity within tumors. Crucially, we experimentally validated the pro-tumorigenic functions of *RAN* and delineated its mechanistic dependence on the PI3K/AKT. Our study found that *RAN* is a promising therapeutic target, which is related to the lactylation in glioma, as well as a new prognostic biomarker.

2. Materials and Methods

2.1 Data Collection and Preprocessing

The Cancer Genome Atlas (TCGA; <https://portal.gdc.cancer.gov/>) [8] and Chinese Glioma Genome Atlas (CGGA; <http://www.cgga.org.cn>) [9] provided us with the bulk RNA-seq data of gliomas, which are in FPKM format, with the clinical data matched with gliomas. The Data were log2-transformed after calculating FPKM value calculation. GEO database (<https://www.ncbi.nlm.nih.gov/gds>, accessions GSE214966 and GSE271379) [10] provided Single-cell RNA sequencing (scRNA-seq). Additionally, spatial transcriptomic data were sourced from GEO accession GSE194329 [11].

2.2 Single-Cell RNA-seq Data Processing

The Seurat package (v4.4.0) in R was used for the data processing, quality control, normalization, dimensionality reduction (PCA, UMAP), clustering, and cell type annotation of scRNA-seq data [12]. Quality control thresholds established were: ‘nFeature_RNA’ between 200 and 9000, ‘nCount_RNA’ between 1000 and 60,000, mitochondrial gene percentage below 12%, ribosomal gene percentage above 3%, hemoglobin gene percentage below 1%. Batch effects were corrected using Harmony [13].

2.3 Lactylation Scoring

A curated total of 332 lactylation-related genes (LRGs, **Supplementary Table 1**) was compiled from the literature [14]. The AUCcell package was utilized to compute a lactylation activity score for each cell based on the enrichment of the LRG set among its expressed genes, quantified as the Area Under the Curve (AUC) [15].

2.4 High-Dimensional Weighted Gene Co-Expression Network Analysis (hdWGCNA)

hdWGCNA was conducted on the malignant cell sub-population (identified via Seurat) using the ‘hdWGCNA’ R package (v0.2.0). Single cells were aggregated into “Meta-cells” to overcome data sparsity. First, genes with high variability were screened. Then, we use the power of the soft threshold of 14 to make the whole network reach a scale-free state. Co-expression modules were subsequently identified using dynamic tree cutting. The module eigengenes (MEs) were then computed, and their relationship with the AUCcell score for lactylation at the cellular level was examined. The module showing the highest correlation with lactylation activity was selected. Genes within this module were intersected with the curated LRG set to obtain candidate LRGs.

2.5 Machine Learning-Based Prognostic Gene Screening

A univariate Cox regression analysis was performed to gauge the prognostic impact of specific lactylation-related genes (LRGs) under consideration. We integrated ten machine learning techniques—LASSO, Ridge, Elastic

Net (ENet), StepCox, survival SVM, CoxBoost, SuperPC, plsRcox, Random Survival Forests (RSF), and Gradient Boosting Machine (GBM)—into a total of 101 unique modeling approaches. These models were developed on the TCGA dataset and subsequently put to the test with the CGGA_mRNAseq_325 dataset. Their effectiveness was measured using the Concordance Index (C-index) as the yardstick. The ENet model ($\alpha = 0.4$), which displayed the highest C-index (0.724), was chosen as the optimal model. Key prognostic genes were determined based on their coefficients in the final Elastic Net model. The prognostic capability of the gene signature was examined utilizing time-dependent Receiver Operating Characteristic (ROC) curves, calibration curves, and Decision Curve Analysis (DCA). A nomogram featuring pivotal genes was developed with the ‘rms’ package (6.3.0) to forecast 1-, 3-, and 5-year general survival rates.

2.6 *RAN*-Related Pathway Enrichment Analysis

We developed the *RAN* protein–protein interaction network employing BioGRID (v4.4.222, Networks module: <https://thebiogrid.org>) [16]. Direct interactors with *RAN* were identified (provided in **Supplementary Table 2**) and examined for Gene Ontology (GO) and Kyoto Encyclopedia of Genes and Genomes (KEGG) pathway enrichment via the clusterProfiler package (4.0) in R. Additionally, Gene Set Enrichment Analysis (GSEA) was carried out using the Hallmark gene sets (MSigDB) across all genes from the TCGA dataset, which were ordered according to their Pearson correlation coefficient relative to *RAN* expression. The resulting enrichment visualizations were generated using ‘ggplot2 (3.5.2)’ and ‘ggprism (0.1.4)’ packages.

2.7 Immune Cell Infiltration Analysis

TCGA glioma specimens were divided into two distinct categories based on *RAN* expression levels, using the median value as the cutoff point. To assess the immune cell landscape, we employed the CIBERSORT method for composition analysis. We applied the ESTIMATE algorithm to determine ImmuneScore, StromalScore, ESTIMATEScore, and TumorPurity. As a follow-up measure, we cross-verified the extent of immune cell infiltration by implementing both ssGSEA and xCell computational approaches. Moreover, the Correlations between *RAN* expression and enrichment scores for specific immune cell subtypes were calculated.

2.8 Spatial Transcriptome Analysis

10X Visium spatial transcriptomic data (GSM5833536) were processed using Seurat for initial clustering. The SpaCET package (0.1.4) was employed for cellular deconvolution to assess the proportions of Malignant, Macrophage, and Endothelial cell types across spatial spots [17]. The malignant cell compartment was isolated, followed by pseudo-temporal ordering of cellular

states using Monocle2 (2.36.0). The spatial distribution of *RAN* expression and its relationship with pseudo-temporal states were then visualized.

2.9 Cell Culture

Human glioma cell lines (U87, LN229, U251) and HEK-293T packaging cells were obtained from the Shanghai Institute of Biological Sciences and Cell Resource Centre (Chinese Academy of Sciences, Shanghai, China). Cells were cultured in Dulbecco’s Modified Eagle Medium (DMEM; Gibco, C11995500BT, Waltham, MA, USA) supplemented with 10% fetal bovine serum (FBS; Gibco, 16000044) and 1% penicillin-streptomycin (Gibco, 15070063) at 37 °C in a humidified atmosphere containing 5% CO₂. All three cell lines used in this study—U87, LN229, U251, and HEK-293T—have undergone STR profiling for authentication and were confirmed to be free of *mycoplasma* contamination.

2.10 Plasmid Construction and Lentiviral Transduction

Short hairpin RNA (shRNA) plasmids targeting *RAN* (sh-*RAN*-1, sh-*RAN*-2) and a non-targeting control shRNA (sh-NC) were synthesized by Uzer Biologics (Guangzhou, China). Lentiviral particles were produced by co-transfecting HEK-293T cells with shRNA plasmids (sh-*RAN*-1, sh-*RAN*-2, or sh-NC) and packaging plasmids (pRV-Rev, pMDLg, pRRE, VSV-G) using Lipofectamine 3000. Glioma cell lines were infected with lentivirus-containing supernatant supplemented with 8 µg/mL polybrene for 24 hours. Transfected cells underwent 72-hour puromycin selection at 2 µg/mL and were confirmed by assessing GFP expression and performing qRT-PCR/Western blot analyses.

2.11 RNA Extraction, Reverse Transcription, and Quantitative Real-Time PCR (qRT-PCR)

RNA extracted from glioma cells with Trizol (Thermo Scientific, 15596018, Waltham, MA, USA) and chloroform was then utilized to create cDNA libraries via a one-step reverse transcription process. qRT-PCR was performed for 40 cycles using the following procedure: 95 °C for 15 s, 60 °C for 15 s and 72 °C for 45 s. The relative expression levels were calculated using the 2^{−ΔΔCT} method. Expression quantities were determined through the 2^{−ΔΔCT} analytical approach. The primer sequences for qRT-PCR were:

RAN-Forward: 5′-CCACCAGAAGTTGTCATGGA CC-3′,

RAN-Reverse: 5′-CTCCAGCTTCATGGACC-3′,

GAPDH-Forward: 5′-TGACATCAAGAAGGTGGT GAAGCAG-3′,

GAPDH-Reverse: 5′-GTGTCGCTGTTGAAGTCA GAGGAG-3′.

2.12 Western Blotting

To kick off the experiment, we lysed the cells using RIPA buffer from Thermo Scientific, spiked with a protease and phosphatase inhibitor cocktail (Thermo Scientific, 89900) to keep everything intact. We then got a handle on the protein concentration with the BCA protein assay kit (Thermo Scientific, 23227). Equal protein aliquots, ranging from 20 to 30 μg , were run through SDS-PAGE and blotted onto PVDF membranes (Merck Millipore, IPFL85R, Darmstadt, Germany). Next up, we blocked the membranes for an hour at room temperature with either 5% non-fat milk or 5% BSA in TBST—switching to BSA when dealing with phospho-specific antibodies. The primary antibodies were left to do their thing overnight at 4 °C, followed by a one-hour incubation with HRP-conjugated secondary antibodies at room temperature. Finally, protein bands were brought to light using enhanced chemiluminescence (ECL) reagent from Meilunbio (MA0186) and crunched the numbers with ImageJ software (version 1.53a, NIH, MD, USA). Antibodies: Anti-*RAN* (Proteintech, 10469, 1:1000, Wuhan, Hubei, China), Anti-AKT (Abmart, T55561, 1:1000, Shanghai, China), Anti-Phospho-Akt (Ser473) (Abmart, T40067, 1:1000, Shanghai, China), Anti-PI3 Kinase p85 (Abmart, T40064, 1:1000, Shanghai, China), Anti- β -actin (Abcam, ab78078, 1:1000, Cambridge, UK) and HRP-conjugated Goat Anti-Rabbit IgG (Biosharp, BL003A, 1:5000, Shanghai, China).

2.13 Cell Proliferation Assay (CCK-8)

Cells (1000 cells/well) were seeded in 96-well plates. Cell viability was assessed at days 0, 1, 3, 5, and 7 using the Cell Counting Kit-8 (CCK-8; MCE, HYK0301, Monmouth, NJ, USA). In summary, 100 μL of the medium with 10% CCK-8 was introduced into each well, followed by an incubation period of 75 min at 37 °C. Subsequently, the absorbance at 450 nm was assessed via a microplate reader (Thermo Scientific, Waltham, MA, USA).

2.14 Colony Formation Assay

Cells (LN229: 1500 cells/well; U251: 1200 cells/well) were seeded in 6-well plates (NEST) and cultured for 14 days, with medium replaced every 5 days. Colonies (>50 cells) were fixed with 4% paraformaldehyde (Solarbio, p1110, Beijing, China) for 20 min and stained with 2.5% crystal violet solution (Meilunbio, MA0148, Dalian, Liaoning, China) for 15 min. Stained colonies were photographed and counted manually.

2.15 Transwell Migration and Invasion Assays

Invasion: the cells were starved of serum for 24 h. Then, 25,000 cells were seeded into the upper compartment of a Transwell insert (which had an 8 μm filter; Corning, 3422, NY, USA) using just 100 μL of serum-free media. The bottom chamber got 500 microliters of all-in-one medium that was 10% FBS. After a 48-hour wait, any cells

that hadn't moved were cleaned off the top with a cotton ball. The cells that had moved down were set with 4% paraformaldehyde, stained with 1% crystal violet, and documented under a microscope (Olympus, Tokyo, Japan). We counted them across five different spots on each insert.

Invasion: Matrigel from Corning (Product Code: 354234) was thinned out at a ratio of 1:8 in serum-free DMEM, and then it was applied to the top of the Transwell inserts, left to set for two hours at body temperature (37 °C). A cell concentration of 2.5×10^5 cells was seeded onto this Matrigel foundation, using just 100 μL of serum-free medium. The rest of the process followed the standard migration protocol.

2.16 Wound Healing Assay

The cells were sown into six-well dishes and allowed to thrive until they achieved about 80 to 90 percent of the plate's coverage. We then employed a sterile pipette tip to incise a clean, unbroken "wound" through the cellular layer. Post-wounding, the plates were rinsed thoroughly with phosphate-buffered saline to clear out any dislodged cells or gunk, after which they were topped up with fresh medium containing 2 percent fetal bovine serum. Wound closure was monitored at 0, 24, and 48 h by imaging the same marked locations under a microscope. The wound healing area was quantified using ImageJ. Wound healing rate (%) = [(Initial wound area – Remaining wound area at time T) / Initial wound area] \times 100%.

2.17 Cell Immunofluorescence Staining (EdU)

Cells were incubated with 10 μM EdU (Beyotime, C0078S, Shanghai, China) for 2 h. Cells were fixed with 4% PFA for 20 min, permeabilized with 0.1% Triton X-100 in PBS for 15 min, and then washed. EdU incorporation was detected using the Click-iT EdU Alexa Fluor 488 Imaging Kit according to the manufacturer's instructions. Nuclei were counterstained with DAPI (Solarbio, S2110). Images were acquired using an inverted fluorescence microscope (Leica, Wetzlar, German).

2.18 Statistical Analysis

The statistical processing was carried out with R software (version 4.3.3, R Foundation for Statistical Computing, Vienna, Austria) and GraphPad Prism (version 8.0.2, GraphPad Software, San Diego, CA, USA). Results are reported as averages accompanied by standard deviations (SD) from a minimum of three separate trials. For comparing the two groups, we employed Student's *t*-test. Survival outcomes were evaluated through Kaplan-Meier plots and log-rank testing. Relationships between variables were examined using either Pearson or Spearman correlation coefficients, depending on which was more suitable for the data. A *p*-value < 0.05 was considered statistically significant (**p* < 0.05 , ***p* < 0.01 , ****p* < 0.001).

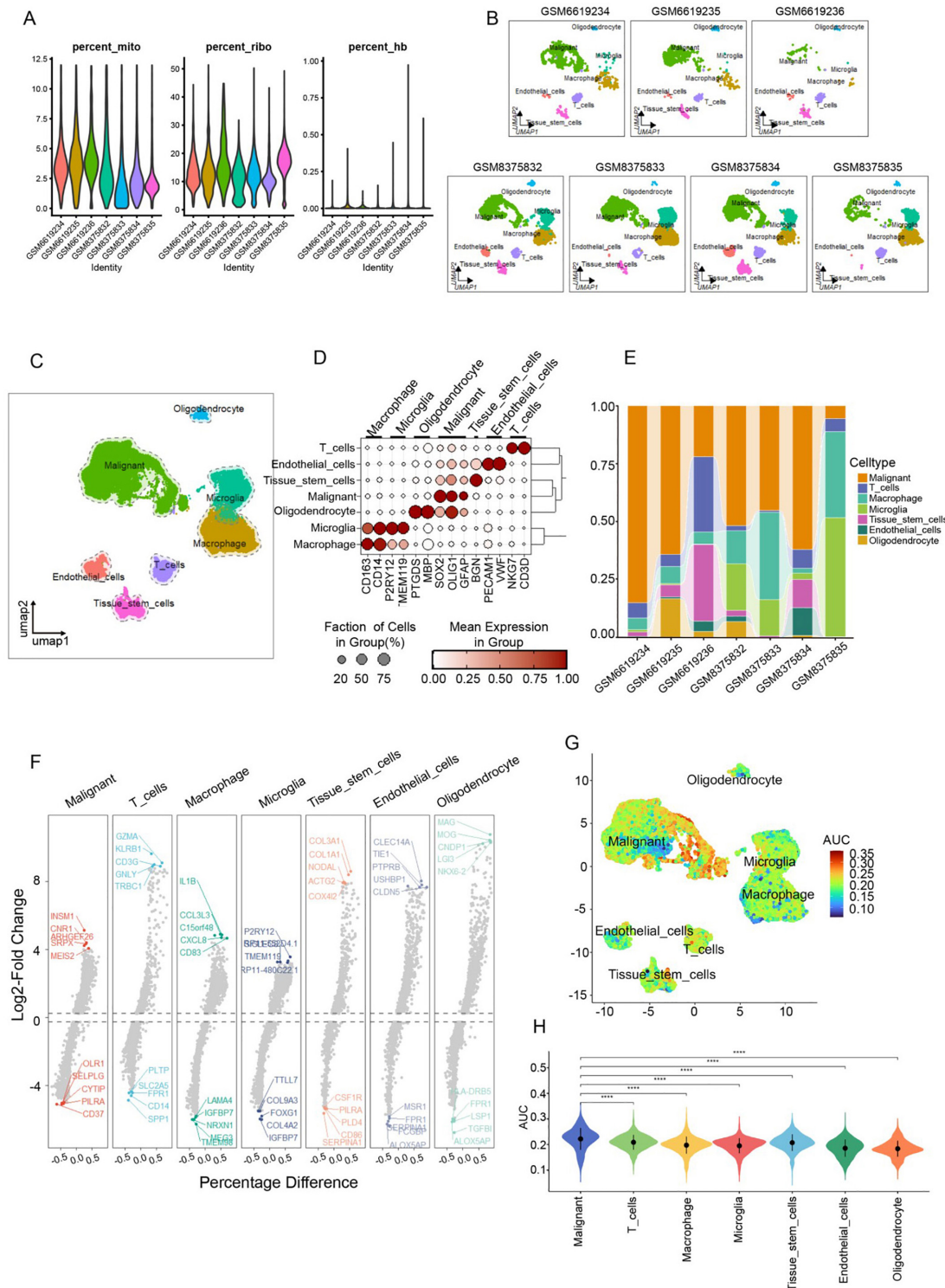


Fig. 1. Cell type identification and cell lactylation degree calculation in single-cell RNA sequencing. (A) Violin illustrations displaying mitochondrial, ribosomal, and hemoglobin gene expression percentages across various sample groups. (B) Uniform Manifold Approximation and Projection (UMAP) visuals derived from single-cell RNA sequencing analyses across multiple specimens. (C) UMAP visualization presenting cell cluster annotations as identified through single-cell transcriptomic profiling. (D) Bubble diagram illustrating marker gene expressions characteristic of distinct cellular phenotypes. (E) Bar graph representing the proportion of cells from each sample categorized into different cellular classifications. (F) Volcano plots highlighting gene expression disparities among various cell types. (G) UMAP plot depicting the lactylation activity levels across different cell populations, quantified via the AUCell computational method. (H) Violin graphics displaying lactylation-related AUCell enrichment scores for various cellular classifications (**** $p < 0.0001$).

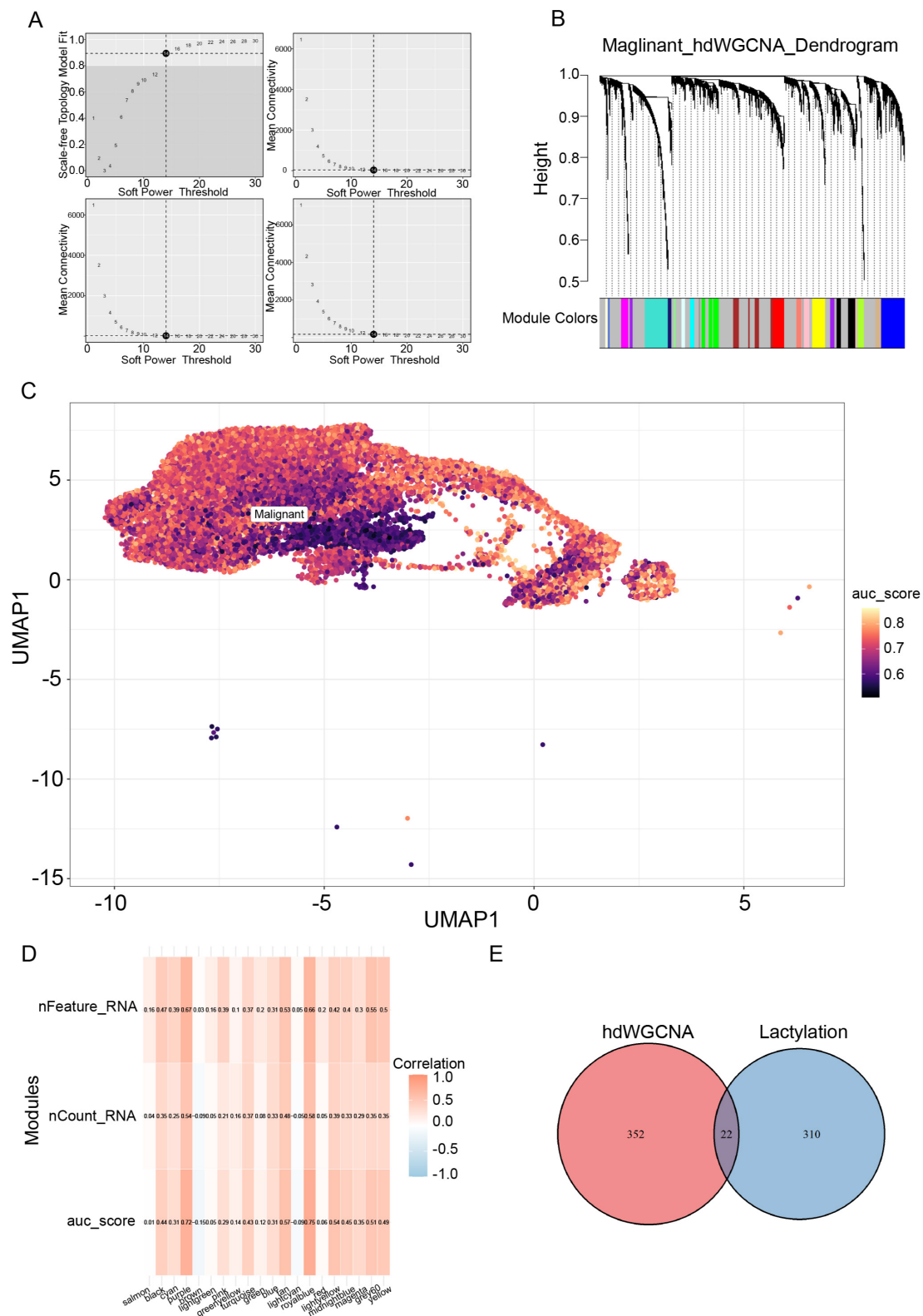


Fig. 2. High-dimensional Weighted Gene Co-expression Network Analysis of differential genes in glioma malignant cells and lactylation AUCell scores of Malignancy. (A) Scatter plots illustrating the scale-free topology model fit and mean connectivity as a function of the soft power threshold. (B) Hierarchical clustering dendrogram of gene expression data, with branches colored according to module assignments. (C) UMAP plot depicting the lactylation score for each malignant cell. (D) The heatmap shows the correlation between different modules and lactic acidification. (E) Venn diagram showing gene intersections from hdWGCNA analysis.

3. Results

3.1 Identification of Cell Types and Calculation of Lactylation Scores

To examine LRGs' possible roles in glioma development, we evaluated single-cell sequencing data from GSE214966 and GSE271379. Following quality control, cells with mitochondrial gene expression <12%, ribosomal gene expression >3%, and hemoglobin gene expression <1% were selected (Fig. 1A), resulting in 31,491 cells retained. Following the Seurat standard workflow, we merged and processed the multi-batch single-cell samples (Fig. 1B), then dimension-reduced and clustered them into seven cell clusters: T cells, endothelial cells, Tissue Stem Cells, Malignant cells, Microglia, Macrophages, and Oligodendrocytes (Fig. 1C). Bubble diagrams depicted the manifestation and distinctiveness of cell-type-specific marker genes (Fig. 1D). These cell types had different proportions in different samples (Fig. 1E), and volcano plots showed significant differences in gene expression between different cell types (Fig. 1F).

Using the AUCell algorithm with all 332 lactylation-related genes, we computed the lactylation score for each malignant cell. The results showed that lactylation alterations were significantly enriched in tumor cells and immune cells, with tumor malignant cells scoring the highest, followed by T-cells and macrophages and microglia, while other non-immune cell types had the lowest (Fig. 1G,H).

3.2 Identification of Lactylation-Related Gene Co-Expression Modules Among Glioma Cells

When the soft threshold of the scale-free topological model was set to 14, the scale-free network was constructed for the best connectivity (Fig. 2A). The clustering dendrogram identified a total of 20 different modules, and genes with high interconnectivity were grouped into the same module (Fig. 2B). Subsequently, we performed individual lactylation scoring on the malignant cell population using the AUCell algorithm (Fig. 2C), and among the 20 co-expressed modules, the royal blue module was the most correlated with the lactylation scoring trait (correlation = 0.75) (Fig. 2D). Taking the intersection of the genes obtained from the above royal blue module with our lactylation gene set, the 22 genes most associated with lactylation were obtained (Fig. 2E).

3.3 Prognostic Assessment and Screening of Lactylation-Related Genes

To further identify the core co-expressed genes from the 22 LRGs, the training set was composed of the TCGA glioma data and the CGGA_mRNAseq_325 was used for validation. We employed various machine learning combinatorial approaches and constructed multiple predictive combinations, using the C-index to evaluate their efficacy. The ENET model ($\alpha = 0.4$), which achieved the highest C-index (0.724), was ultimately selected as the op-

timal model (Fig. 3A). Subsequently, lactylation-related genes underwent univariate Cox analysis (Fig. 3B) to assess their prognostic relevance in TCGA glioma data. Then, we selected the best model (ENet) to optimize the selection and verified the robustness of this gene subset with Lambda plots (Fig. 3C,D), and finally obtained the six key lactylation-associated genes, namely, *PDAP1*, *ALYREF*, *CBX3*, *MAGOH*, *RAN*, and *TMSB4X* (using the TCGA glioma dataset). The ROC curves as well as the Calibration curves confirmed the robust and accurate predictive ability of the model, with aucs of 0.774, 0.809, and 0.829 for 1-, 3-, and 5-year OS in the train set and aucs of 0.752, 0.869, and 0.884 for 1-, 3-, and 5-year OS in the test set, respectively, and the Decision Curve Analysis (DCA) further demonstrated that the model had higher high net clinical benefit value of the model (using the CGGA.mRNAseq_693 dataset) (Fig. 3E,F).

Based on the final key genes obtained, we constructed a nomogram to predict patient survival (using the CGGA.mRNAseq_693 dataset) (Fig. 3G). Similarly, we evaluated this nomogram using the tROC curve and the calibration curve as the evaluation criteria, and their AUC at 1, 3, and 5 years were 0.812, 0.855, and 0.876, respectively (using the CGGA.mRNAseq_325 dataset) (Fig. 3I). Additionally, the calibration graph revealed a robust correlation between the model's forecasts and real data points, showcasing its proficiency in precise risk assessment (Fig. 3H). Overall, the nomogram model developed with key lactylation-related genes as evaluation criteria has a robust and accurate prediction ability, which also proves that the screened LRGs can be prognostic biomarkers.

3.4 RAN-Related Gene Enrichment Analysis and Survival Analysis

Among the last six hub genes we identified, all except the *RAN* gene have been experimentally validated to regulate glioma progression [18–22]. Furthermore, the *RAN* gene also exhibits specific expression in gliomas (Fig. 4F,G). So we concentrated on the *RAN* gene for subsequent investigation and experimental confirmation. To investigate how *RAN* contributes to cancer development, we extracted the top 499 *RAN*-associated genes from BioGRID4.4 (Supplementary Table 2) to constructed a relevant network diagram (Fig. 4B). GO and KEGG analyses revealed *RAN*'s critical function in nuclear import processes, nuclear transport and nucleoplasmic transport, including NLS-dependent nuclear import of proteins, and maintenance of nuclear pore structure and function. It also has ubiquitin-protein ligase binding and nuclear import signaling receptor activities that regulate pathways such as multispecies longevity and shigellosis, and is an important regulator of nuclear transport (Fig. 4A). Subsequently, to explore the pathways through which pathways *RAN* primarily plays a regulatory role in cancer, we performed Pearson correlation analysis of all genes in the TCGA dataset

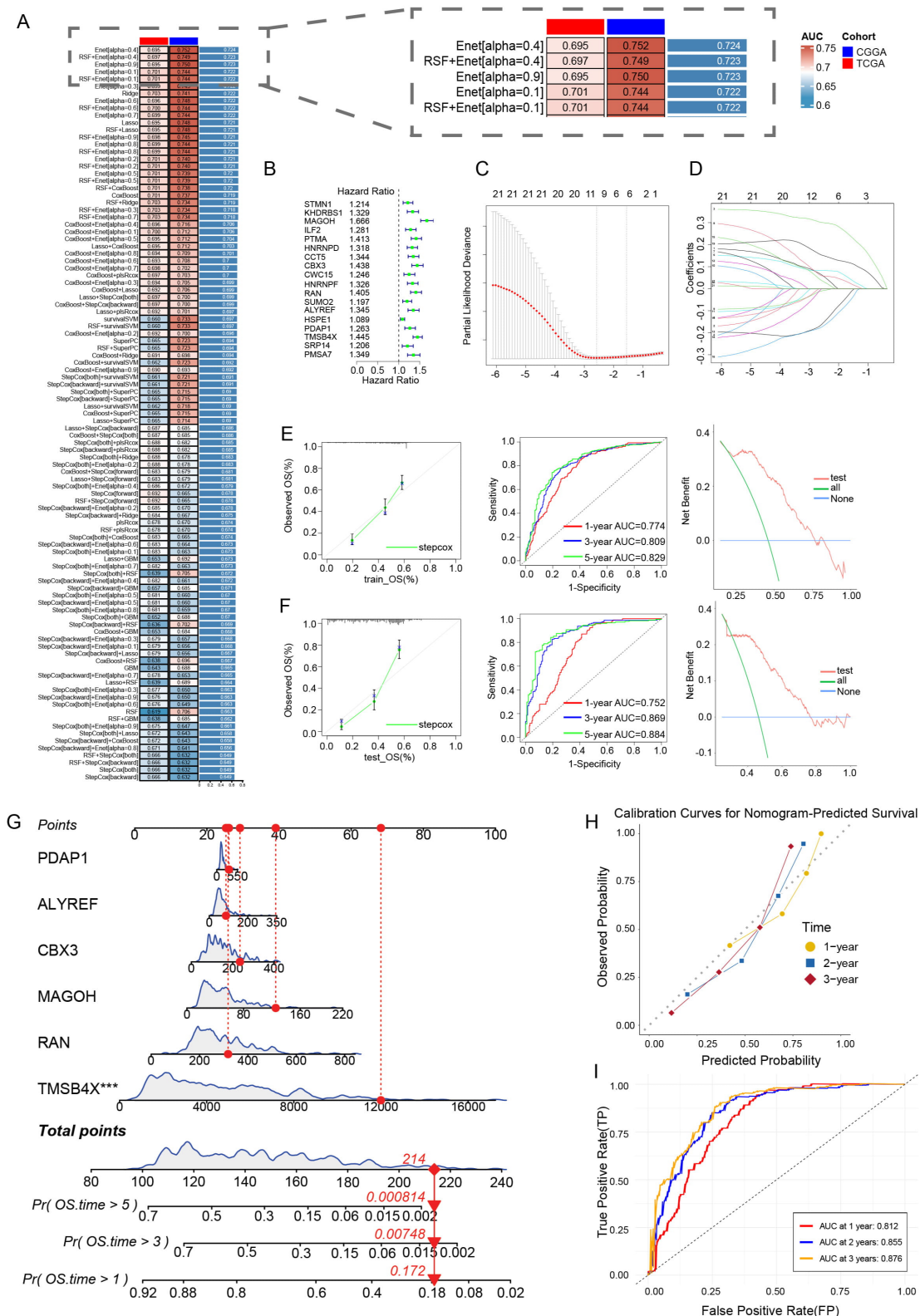


Fig. 3. Machine learning screening of prognostic-related lactylation-related genes (LRGs) and nomogram model construction. (A) Heatmap showing the c-index of multiple models derived from combinations of different machine learning algorithms. (B) Forest diagram depicting risk ratios and statistical probabilities of multiple genes. (C) Lambda distribution chart of risk coefficients in the Lasso model. (D) Six non-zero coefficient genes were obtained from the Lasso regression analysis. (E,F) Calibration curve, Receiver Operating Characteristic (ROC) curves, and Decision Curve Analysis (DCA) collectively validate the performance of the ENet model in the train and test cohorts. (G) Nomogram constructed from hub LRGs. (H,I) Calibration curve, ROC curves for validating nomogram models.

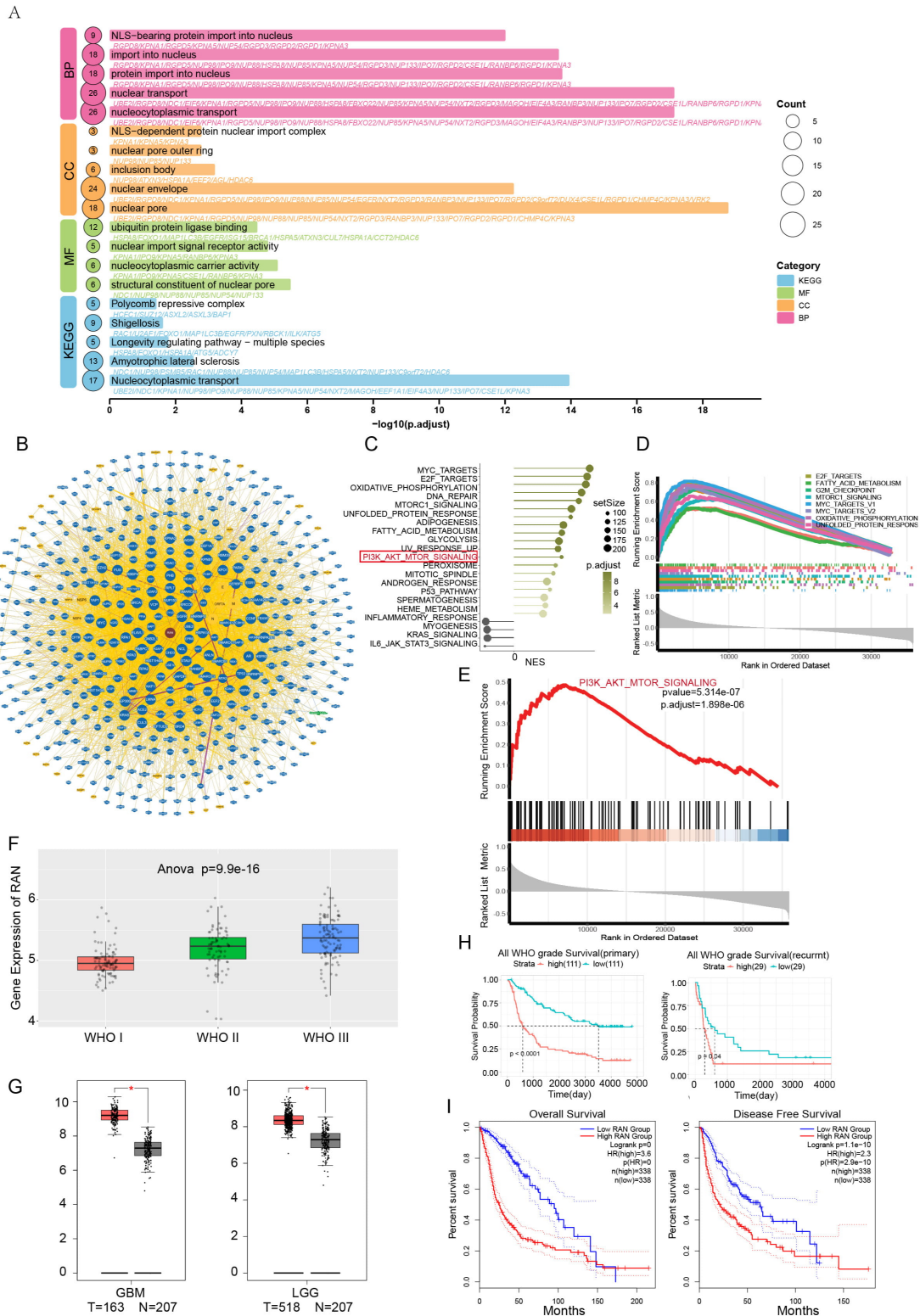


Fig. 4. Functional enrichment analysis and prognostic analysis of gene *RAN*. (A) Functional Enrichment Analysis of the *RAN*. (B) Protein interaction map for *RAN* obtained from the BIOGRID. (C) GSEA enrichment analysis bar chart for *RAN*. The red box is the signaling pathway we selected. (D) GSEA enrichment pathway map of the top 10 pathways in the *RAN*-related GSEA enrichment analysis. (E) GSEA enrichment analysis chart of the PI3K/AKT pathway. (F) *RAN* gene expression levels in glioma at different WHO grades compared with normal tissue (CGGA). (G) Expression levels of *RAN* in GBM and LGG (TCGA) (* $p < 0.05$). (H) Survival analysis of the *RAN* gene in initial and relapsed brain tumors (CGGA). (I) *RAN* expression levels in LGG and GBM compared with normal tissue (TCGA).

with *RAN*, which were ranked in order according to their correlation, and then performed GSEA analysis with the hallmark's gene set as the annotated gene set (Fig. 4C,D). The enrichment results showed that the main enriched pathways included PI3K-AKT-mTOR signalling, MYC targets, E2F targets, oxidative phosphorylation and G2M checkpoints, suggesting that *RAN* potentially taking center stage in governing cellular growth, division, and metabolic processes. Moreover, in aggressive cancers like non-small cell lung cancer, *RAN* has been found to pull the strings behind tumor cell multiplication and spread by tapping into the PI3K/AKT signaling cascade, as highlighted in references [23,24]. This pathway was also significantly enriched in GSEA ($p_{\text{adjust}} = 1.698 \times 10^{-6}$) (Fig. 4E), then PI3K-AKT pathway was chosen for further mechanistic studies. In addition, analysis of the GEPIA and CGGA databases (CGGA_mRNAseq_325) revealed that *RAN* exhibited substantially increased expression in each WHO grade of gliomas compared with normal tissues, with expression levels increasing in parallel with glioma malignancy (Fig. 4F,G). Survival analysis further indicated that patients with low *RAN* expression exhibited the most favorable overall survival, whereas those with high *RAN* expression showed the poorest prognosis (Fig. 4H,I). Collectively, these findings suggest that *RAN* potentially drives tumor progression via the PI3K-AKT signaling axis, supporting its pro-tumorigenic function in glioma.

3.5 Correlation Between *RAN* and Immune Infiltration

To study immune infiltration in gliomas and to compare the immune cell composition between patient subgroups stratified by high versus low *RAN* expression, we evaluated immune cell infiltration levels in glioma patients by analyzing TCGA datasets with the CIBERSORT. The heatmap (Fig. 5A) illustrates the distribution patterns of 22 immune cell types between patient groups categorized by *RAN* expression levels. When it comes to the IMMUNE, STROMAL, and ESTIMATE metrics, these values were through the roof in the cohort with lower *RAN* expression compared to their counterparts in the high-expression group ($p < 0.001$), implying that dysregulated *RAN* expression could contribute to substantial alterations in the immune microenvironment (Fig. 5B). Subsequently, we employed the ssGSEA and XCell analytical approaches to gauge the extent of immune cell penetration in each glioma sample, uncovering that the subgroup with diminished *RAN* expression showed a marked uptick in immune cell presence. This included a diverse array such as activated B cells, CD4⁺ T cells in action, natural killer T cells, and microglia, among others (Fig. 5C,D). We selected the top 6 immune cell types with correlation in ssGSVA for demonstration (Fig. 5E), *RAN* expression with Class-switched memory B-cells ($R = -0.34$, $p = 1.4 \times 10^{-5}$), Th2 cells ($R = 0.65$, $p < 2.2 \times 10^{-16}$), Epithelial cells ($R = -0.33$, $p = 2 \times 10^{-5}$), B-cells ($R = -0.33$, $p = 3.4 \times 10^{-5}$), Tregs ($R = -0.32$, $p =$

4.7×10^{-5}), and Eosinophils ($R = -0.36$, $p = 5 \times 10^{-6}$) were negatively correlated with enrichment scores. The results indicate *RAN* shapes the tumor microenvironment and could serve as a significant immunotherapy biomarker.

3.6 Spatial and Temporal Specificity of *RAN* in Glioma Tissues

Prior research indicates fluctuating *RAN* levels occur in various cell types across time. To explore the temporal and spatial heterogeneity of the *RAN* in glioma tissues, we used the Seurat process to perform preliminary reads on GSE194329 and clustered them into six classes (Fig. 6A,B). The initial clustering of cells was analyzed using the SpaCET package which categorized them into three cell classes “Malignant”, “Macrophage”, and “Endothelial” (Fig. 6C). From the analysis, the Malignant cell cluster was isolated and the Monocle2 algorithm was used to propose the time series calculation, and it was identified that cluster 1 in the Malignant cell cluster transformed to cluster 3 over time (Fig. 6E), and the genes in different clusters showed diametrically opposite expression trends in the process of evolution (Fig. 6F). The expression of *RAN* decreased with the temporal progression of tumor cells (Fig. 6D), suggesting that the *RAN* is temporally heterogeneous in tumor tissues. Subsequently we marked the process of tumor cell evolution (Fig. 6G) and the spatial distribution of *RAN* expression (Fig. 6H) in the “Malignant section” of the tumor, and visualization indicated decreased *RAN* expression with the progression of evolution. Subsequently, Malignant cells were further convolved to obtain the malignant cell state, “Malignant cell state A”, “Malignant cell state B” (Fig. 6I). *RAN* expression was significantly lower in state A compared to state B, confirming spatial heterogeneity of the gene. These results also indicate that *RAN* exerts control over the progression of glioma cells.

3.7 *RAN* Knockdown Significantly Inhibits the Proliferation of Glioma

Bioinformatics analysis suggested that *RAN* could regulate various biological behaviors in gliomas. To explore *RAN* function, we employed shRNA to create a knockdown model in U87, LN229 and U251. We verified efficiency of the knockdown using qPCR and WB analysis (Fig. 7A,B), and selected sh-*RAN*-1 for experiments. The CCK-8 method was employed to measure the growth of the glioma cell lines under investigation at day 0, 1, 3, 5 and 7 post-transfection. The findings showed a substantial decrease in the growth potential of the knockdown group when contrasted with the control group, as illustrated in Fig. 7C. Moreover, the colony formation tests revealed a marked reduction in the number of colonies for both the LN229 and U251 cell lines post-*RAN* knockdown, when compared to the untreated cells (Fig. 7D,E). Pictures of the EdU fluorescence staining assays (Fig. 7F–H) further confirmed these findings, showing that fluorescence intensity

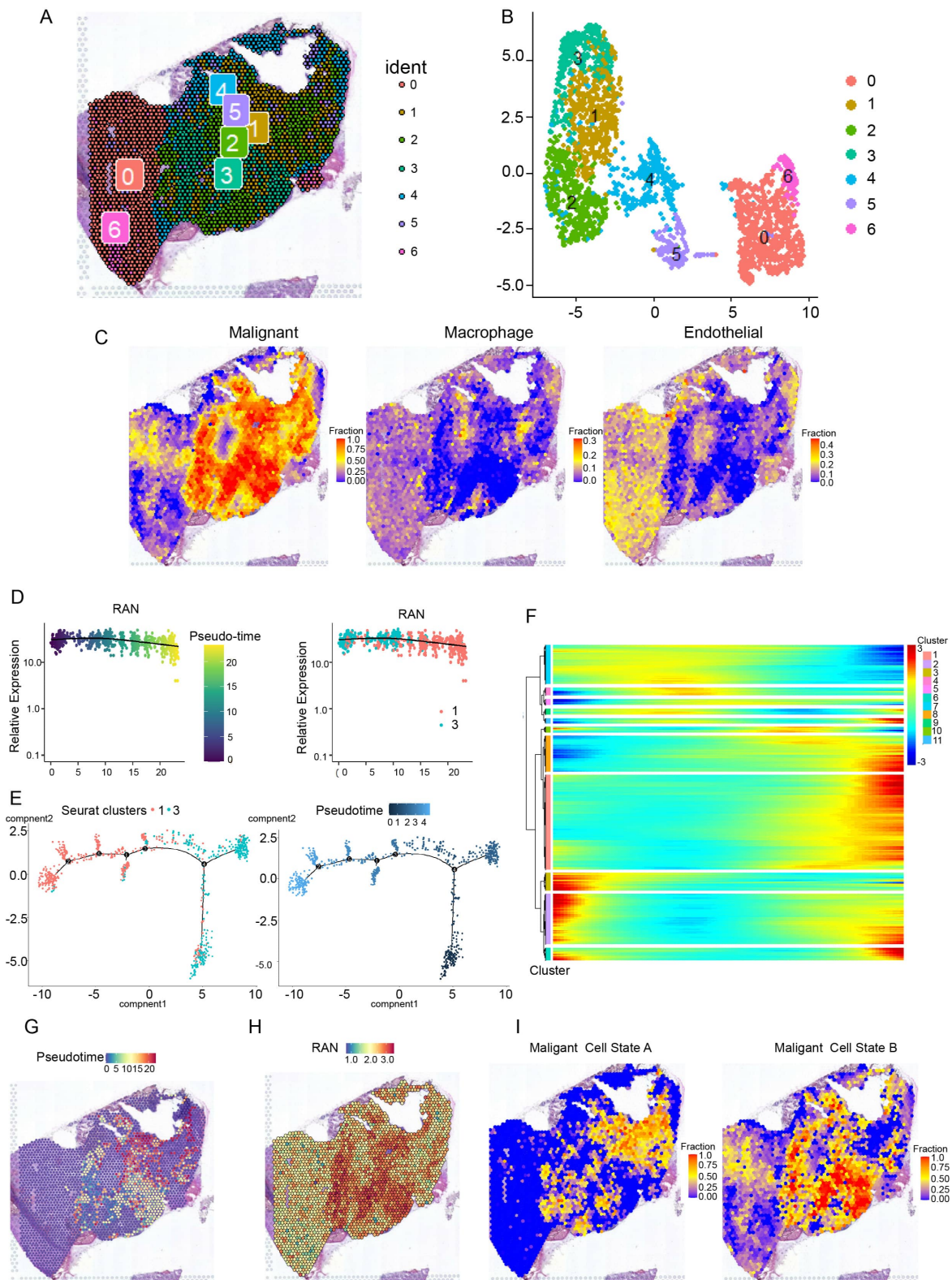


Fig. 6. Temporal-spatial expression specificity of *RAN* in spatial transcriptomes. (A,B) The UMAP plot of single-cell transcriptomic data and display of the corresponding region in the pathological section. (C) The distribution of the three cell types “Malignant”, “Macrophage”, and “Endothelial” in pathological sections, as reconstructed by SpaCET deconvolution. (D) *RAN* expression changes with cell development. (E) The development of malignant cell clusters over time. (F) Gene expression dynamics across developmentally distinct clusters identified by monocle2. (G) Spatial development process of tumor cells. (H) Spatial distribution of *RAN* expression. (I) Malignant state of malignant cells derived from SpaCET deconvolution.

of the sh-*RAN* group was significantly decreased compared with that of the sh-NC group in both U87 and U251 cell lines. This suggests that *RAN* knockdown slowed DNA synthesis rate was significantly slowed down after knockdown of *RAN*, indicating its importance in the proliferation of glioma.

Furthermore, the sh-*RAN* group exhibited markedly reduced scratch recovery compared to the sh-NC group for both U251 and LN229 cells, with the difference being particularly pronounced at the 48-hours marks (Fig. 7I–K). Transwell chamber assays for invasion and migration also revealed that the count of cells that migrated through the lower chamber significantly decreased post lockdown (Fig. 7L–N), and the tumor cells' migration and invasion capabilities were markedly diminished. This suggests that *RAN* simultaneously regulates tumor cell invasion and migration.

3.8 Silencing of the *RAN* Gene Suppresses the Malignant Progression of Glioma Through Inhibition of the PI3K/AKT/mTOR Signaling Pathway

Our prior functional enrichment analysis of the *RAN* revealed its regulatory influence on biological features of glioma cells via the PI3K/AKT signaling cascade (Fig. 4D). Consequently, we directed subsequent investigations on this pathway to delineate the molecular mechanism involving *RAN*. Initially, in U251 cells, we observed a similar downregulation of the pathway following *RAN* knockdown (Fig. 8A,B). To determine if *RAN* knockdown's suppression of glioma activity could be counteracted by PI3K/AKT pathway activation, we employed SC79, a pathway activator. WB analysis showed that there was a significant reversion of p-AKT levels after introducing PI3K/AKT pathway activator, restoring it to the levels comparable to the non-knocked-down control (Fig. 8C,D). Moreover, our phenotypic investigations showed that glioma cells with *RAN* knockdown, when also treated with the pathway activator, demonstrated markedly enhanced proliferation and colony formation capabilities—surpassing the single knockdown group and essentially matching the control group's performance (Fig. 8E–G). Moreover, both scratch wound healing and transwell migration assays revealed that introducing the PI3K/AKT activator completely counteracted the diminished migratory and invasive capacities triggered by *RAN* suppression (Fig. 8H–K). Collectively, these findings strongly suggest that *RAN* knockdown curtails the aggressive characteristics of glioma cells by inhibiting the PI3K/AKT signaling pathway.

4. Discussion

Glioma is the most prevalent primary malignant brain tumor and is characterized by notably poor survival outcomes and significant resistance to conventional therapeutic approaches. Glioblastoma (GBM), representing the most aggressive subtype of glioma, currently lacks well-

defined molecular targets and established mechanistic treatment strategies [25]. This highlights the critical need for more reliable and robust biological markers for glioma classification. Recent evidence emphasizes the significance of such markers; for example, alterations in IDH1 and IDH2 represent early molecular changes that primarily arise in lower-grade gliomas, whereas glioblastomas generally exhibit *IDH*-wildtype status [26]. Previous studies have established that mutations in epigenetically regulated genes constitute key factors driving divergent prognostic clinical features across glioma subtypes [27]. These epigenetic modifications represent significant molecular hallmarks and promising therapeutic targets for clinical diagnosis and treatment. One such recently discovered modification is lactylation, which plays important roles in cancer progression and immune microenvironment regulation, and other pathological states. However, research on lactylation-related genes (LRGs) in gliomas remains scarce, and existing algorithms and data collection for molecular markers are relatively homogeneous, lacking systematic and robust approaches.

This work implemented an integrated framework that concurrently utilized single-cell RNA sequencing (scRNA-seq) and bulk transcriptomic profiling, complemented by diverse computational methods, to delineate lactylation-linked genes serving as molecular indicators in glioma. A prognostic signature was then developed. First, we performed clustering and annotation of single-cell populations, utilizing the AUCCell algorithm to score lactylation levels specifically within malignant tumor cell populations. Then, we applied the hdWGCNA algorithm to identify gene modules that were most strongly correlated with the lactylation trait. The intersection of these modules with established LRGs yielded key lactylation-associated genes. To further refine this set and select the LRGs most relevant to prognosis, we implemented 101 distinct combinations of machine learning algorithms. This rigorous process culminated in the identification of six key LRGs, which were incorporated into a nomogram-based prognostic scoring model. The performance of our prognostic scoring system really hit the mark when put to the test, with calibration plots and time-dependent ROC analysis showing it's right on the money. The predictive power was nothing short of impressive, boasting AUC scores of 0.812, 0.855, and 0.876 for 1, 3, and 5-year windows respectively, proving this tool is truly cut out for the job, respectively. The calibration curves further confirmed the model's accurate predictive capability, robustly validating the high prognostic relevance of the selected genes.

To further validate and explore the biological function of one key candidate, we selected *RAN* for experimental validation and functional analysis. *RAN*, being a member of the Ras GTPase superfamily, regulates spindle formation and nuclear envelope (NE) reassembly, playing a crucial role in mitosis and proliferation of nucleated

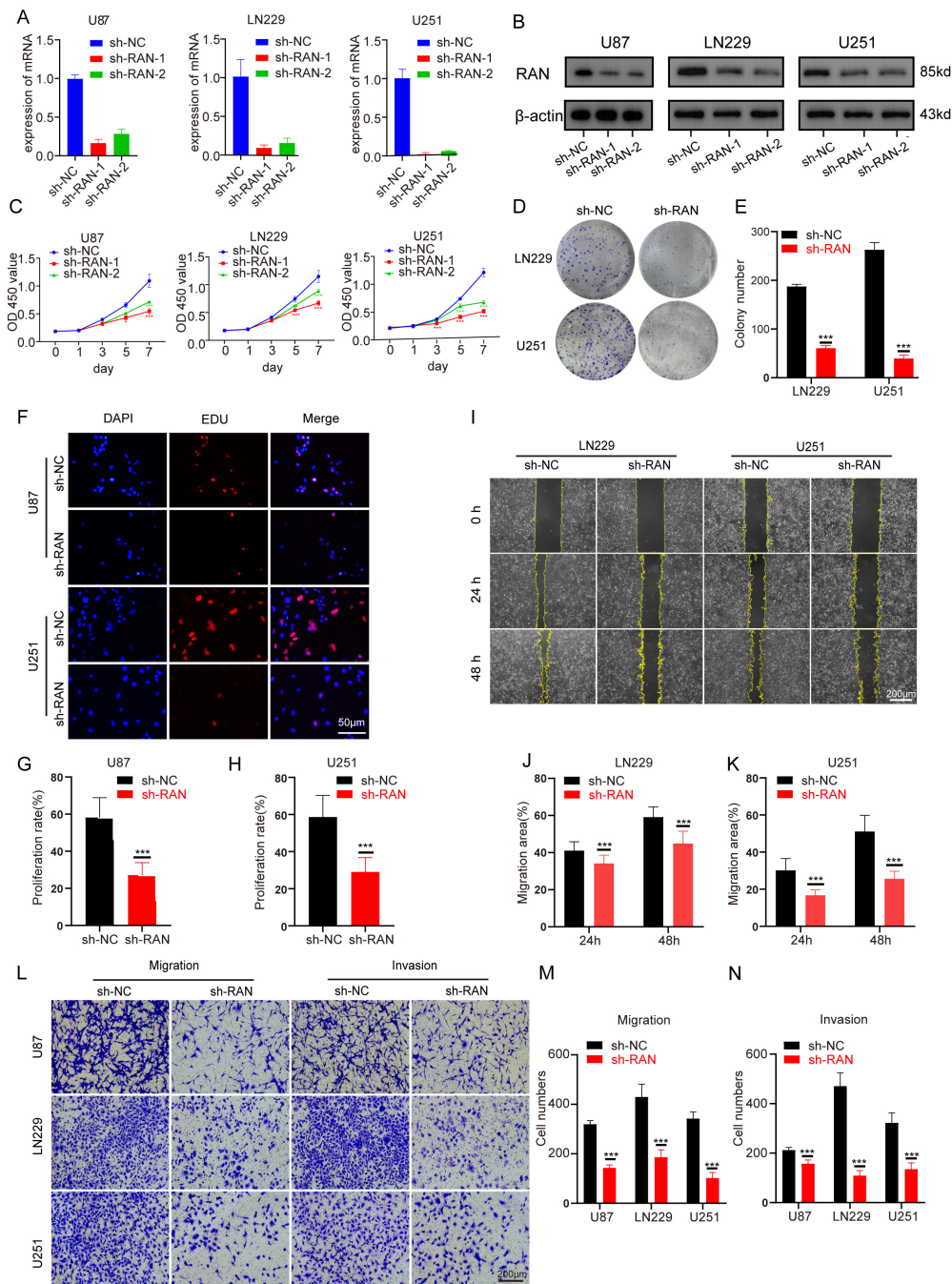


Fig. 7. Effects of *RAN* knockdown on proliferation, migration, and invasion in glioma cells. (A) The knockdown efficiency of *RAN* in U87, LN229, and U251 glioma cells transfected with sh-NC, sh-RAN-1, and sh-RAN-2, as determined by qRT-PCR ($n = 3$). (B) Western blot analysis of *RAN* and β -actin protein levels in U87, LN229, and U251 cells transfected with sh-NC, sh-RAN-1, and sh-RAN-2. β -actin was used as a loading control. (C) Cell proliferation curves of U87, LN229, and U251 cells transfected with sh-NC, sh-RAN-1, and sh-RAN-2, as measured by CCK-8 assay ($n = 5$). (D,E) Colony formation assay of LN229 and U251 cells transfected with sh-NC and sh-RAN. Representative images of colonies are shown. (F–H) EdU incorporation assay of U87, LN229, and U251 cells transfected with sh-NC and sh-RAN ($n = 3$). Three microscopic fields of view were selected for each well. Scale bar: 50 μ m. (I–K) Scratch wound-healing assay of U87, LN229, and U251 cells transfected with sh-NC and sh-RAN ($n = 3$). Representative images at 0 h, 24 h, and 48 h are shown. Migration rate (%) = Migration area / Scratch area \times 100%. Scale bar: 200 μ m. (L–N) Transwell migration and invasion assays of U87, LN229, and U251 cells transfected with sh-NC and sh-RAN ($n = 3$). Three microscopic fields of view were selected from top to bottom in each small chamber to calculate the average number of cells passing through each small chamber. Scale bar: 200 μ m. Data are presented as mean \pm SD. * p < 0.05; ** p < 0.01; *** p < 0.001.

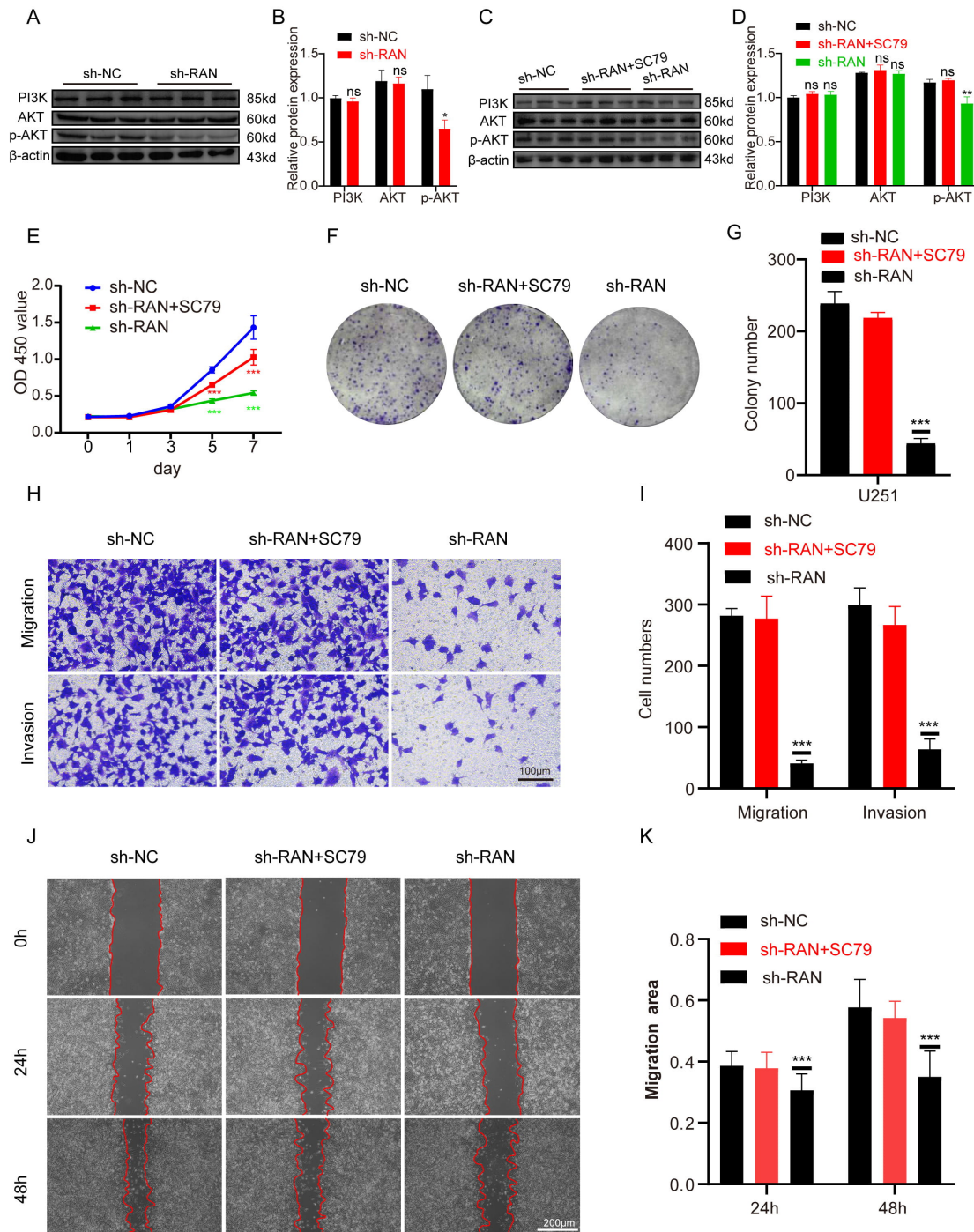


Fig. 8. AKT activator SC79 reverses the inhibitory effect of *RAN* knockdown on malignant biological behavior in glioma. (A,B) Western blot evaluation of PI3K, AKT, and p-AKT expression levels in U251 cells following transfection with either sh-NC or sh-*RAN* constructs. β -actin served as the internal reference protein for normalization across all samples ($n = 3$). (C,D) Assessment of PI3K, AKT, and p-AKT protein expression in U251 cells transfected with sh-NC, sh-*RAN*, and sh-*RAN* plus SC79 treatment using Western blot analysis. β -actin was utilized as the loading control for equal protein loading ($n = 3$). (E) Cell proliferation assay of U251 cells transfected with sh-NC, sh-*RAN*, or sh-*RAN* treated with SC79. The OD450 value was measured at different time points (0–7 days). (F,G) Representative images of colony formation in U251 cells transfected with sh-NC, sh-*RAN*, or sh-*RAN* treated with SC79 ($n = 3$). (H,I) Representative images of migration and invasion assays in U251 cells transfected with sh-NC, sh-*RAN*, or sh-*RAN* treated with SC79. Scale bar: 100 μ m. (J,K) Representative images of wound healing assays in U251 cells transfected with sh-NC, sh-*RAN*, or sh-*RAN* treated with SC79 at 0 h, 24 h, and 48 h ($n = 3$). Migration rate (%) = Migration area / Scratch area \times 100%. Scale bar: 200 μ m. Data are presented as mean \pm SD. ns, no significant; * $p < 0.05$; ** $p < 0.01$; *** $p < 0.001$.

cells [28–31]. Despite its fundamental role, the contribution of *RAN* to glioma pathogenesis remains poorly characterized, motivating its selection as a focal point of our study. To elucidate the pathways and functions associated with *RAN*, we retrieved 499 *RAN*-interacting genes from the BioGRID database for enrichment analysis. The results indicated that *RAN* is central to nuclear import, nuclear transport, and nucleoplasmic transport processes. It is critically involved in NLS-dependent nuclear protein import, maintaining the structure and function of nuclear pores, and governing nucleocytoplasmic transport. To dig deeper into *RAN*'s implications in cancer pathology, we conducted a Pearson correlation analysis across the entire genome, which was then followed by a Hallmark Pathway Gene Set Enrichment Analysis (GSEA) that ordered genes based on their correlation coefficients. This investigative approach uncovered notable enrichment in biological pathways tied to cell division and metabolic processes, specifically highlighting MYC target genes, E2F-regulated genes, the PI3K/AKT/mTOR signaling cascade, and oxidative phosphorylation mechanisms. Further laboratory experiments ultimately substantiated that *RAN* plays a pivotal role in controlling both metastatic movement and cancer cell multiplication.

The PI3K/AKT signaling cascade represents a central intracellular transduction pathway mediated by phosphatidylinositol 3kinase (PI3K) and protein kinase B (AKT). This axis regulates vital cellular activities including growth, proliferation, survival, metabolic homeostasis, motility, and angiogenesis. Dysregulation of this pathway is closely associated with tumorigenesis and constitutes a key target for anticancer therapeutics [32,33]. Furthermore, the pathway crosstalks with epigenetic mechanisms, as major epigenetic regulators are modulated—directly or indirectly—by PI3K/AKT signaling, contributing to its oncogenic effects [34]. The identification of *RAN*, a lactylation-associated gene, as enriched in PI3K/AKT signaling suggests a potential high correlation. Furthermore, *RAN*-mediated regulation of cancer cell biology via the PI3K/AKT pathway has been documented in other malignancies. Therefore, we investigated this molecular mechanism in glioma and successfully demonstrated that *RAN* regulates glioma cell behaviors, particularly proliferation and migration, through modulation of the PI3K/AKT pathway.

Cancer represents an intricate cellular network encompassing malignant and various benign components, with the tumor microenvironment (TME) serving as a fundamental contributor to pathogenesis [35]. Immune microenvironment alterations are particularly significant in glioma development and treatment response [36]. Recent study has demonstrated that *RAN* modulates lipid metabolism through the nuclear export of phosphoAMPK, thereby promoting tumor resistance to immunotherapy, and suppresses MHC-associated molecules to escape CD8⁺ T cell-mediated

immune surveillance [37]. Consistent with these reports, our data reveal that elevated *RAN* expression correlates with a markedly impaired tumorsuppressive capacity in the immune microenvironment. In contrast, the low *RAN* cohort showed enhanced recruitment of immune effector populations, such as activated B lymphocytes, activated CD4⁺ T cells, natural killer T (NKT) cells, and microglia. This differential immune infiltration profile correlates with the observed worse prognosis in the high *RAN* expression group. Collectively, these data indicate that *RAN* plays a critical role in glioma development by modulating levels of immune cell influx in the tumor microenvironment, thereby promoting an immunosuppressive state.

The small GTPase gene *RAN* functions in diverse cellular processes with strict spatiotemporal specificity and is central to the spatial and temporal organization of vertebrate cells [38]. To investigate potential spatiotemporal organizational differences of *RAN* in gliomas, we analyzed spatial transcriptomic data. The results revealed distinct spatial distribution patterns for *RAN* within glioma tissues, showing notably elevated levels of expression within tumor cells versus other cellular types. Furthermore, *RAN* expression exhibited a decreasing trend with tumor progression. These observations suggest that *RAN* expression is spatiotemporally regulated in gliomas and likely influences the process of tumorigenesis and development.

Finally, while this study identified prognostically significant lactylation-related genes and constructed a robust and efficient prognostic model, several limitations must be acknowledged. First, the LRGs examined here represent non-histone lactylation targets. Despite our examination of how these modifications influence tumor behavior, the exact ways in which lactylation tweaks gene expression or function still fly under the radar. Getting to the bottom of this puzzle will require digging deeper into the mechanics of lactylation and its protein counterparts to unlock their full potential in cancer treatment. Second, our data analysis relied primarily on public databases and lacked corresponding clinical correlative studies integrated with detailed patient information. We plan to address this by collecting and analyzing clinical data in the future. Finally, the screening process across multiple datasets and algorithms inevitably introduces batch effects, and we will further optimize our algorithms to enhance the robustness of the screening procedure.

5. Conclusion

In summary, this integrative multi-omics study establishes lactylation as a key regulator of glioma progression and the TME. We identified and validated *RAN* as a novel lactylation-associated oncogene that drives glioma malignancy primarily through activation of the PI3K/AKT/mTOR pathway. *RAN* serves as a powerful independent prognostic biomarker associated with an immunosuppressive TME and exhibits spatiotemporal hetero-

geneity within tumors. Our findings position *RAN* as a promising therapeutic target for glioma. Targeting *RAN* or its downstream PI3K/AKT effector pathway holds significant potential for improving the dismal prognosis of glioma patients. This study provides a compelling rationale for further investigation into lactylation biology and *RAN*-targeted therapies in glioma.

Availability of Data and Materials

All data used in this paper were obtained from public databases, including GEO, TCGA, and CGGA. Upon reasonable request, the datasets used and analyzed in this study can be provided by the corresponding author.

Author Contributions

SW carried out most of the experiments, data analysis, and drafted the manuscript; FT, HC and JP carried out several experiments; YingZ made figures and tables; JY and YueZ designed the research; SW and JY wrote and edited the manuscript. All authors contributed to editorial changes in the manuscript. All authors read and approved the final manuscript. All authors have participated sufficiently in the work and agreed to be accountable for all aspects of the work.

Ethics Approval and Consent to Participate

Not applicable.

Acknowledgment

We thank the Scientific Research Center of Wenzhou Medical University for providing the confocal microscopy. We are sincerely grateful to those who created and maintained these public databases such as The Cancer Genome Atlas (TCGA) and the Chinese Glioma Genome Atlas (CGGA). Finally, the authors would like to thank all researchers who participated in this study.

Funding

This study was supported by the National Natural Science Foundation of China (No. 82103216) and Zhejiang Province Health Industry Science and Technology Plan General Project (No. 2026771975).

Conflict of Interest

The authors declare no conflict of interest.

Declaration of AI and AI-Assisted Technologies in the Writing Process

During the preparation of this work, the authors used ChatGPT in order to check spelling and grammar. After using this tool, the authors reviewed and edited the content as needed and take full responsibility for the content of the publication.

Supplementary Material

Supplementary material associated with this article can be found, in the online version, at <https://doi.org/10.31083/FBL46765>.

References

- [1] Bale TA, Rosenblum MK. The 2021 WHO Classification of Tumors of the Central Nervous System: An update on pediatric low-grade gliomas and glioneuronal tumors. *Brain Pathology*. 2022; 32: e13060. <https://doi.org/10.1111/bpa.13060>.
- [2] Stupp R, Mason WP, van den Bent MJ, Weller M, Fisher B, Taphoorn MJB, *et al*. Radiotherapy plus concomitant and adjuvant temozolomide for glioblastoma. *The New England Journal of Medicine*. 2005; 352: 987–996. <https://doi.org/10.1056/NEJMoa043330>.
- [3] Louis DN, Perry A, Wesseling P, Brat DJ, Cree IA, Figarella-Branger D, *et al*. The 2021 WHO Classification of Tumors of the Central Nervous System: a summary. *Neuro-oncology*. 2021; 23: 1231–1251. <https://doi.org/10.1093/neuonc/noab106>.
- [4] Li H, Sun L, Gao P, Hu H. Lactylation in cancer: Current understanding and challenges. *Cancer Cell*. 2024; 42: 1803–1807. <https://doi.org/10.1016/j.ccell.2024.09.006>.
- [5] Zhu R, Ye X, Lu X, Xiao L, Yuan M, Zhao H, *et al*. ACS2 acts as a lactyl-CoA synthetase and couples KAT2A to function as a lactyltransferase for histone lactylation and tumor immune evasion. *Cell Metabolism*. 2025; 37: 361–376.e7. <https://doi.org/10.1016/j.cmet.2024.10.015>.
- [6] Li G, Wang D, Zhai Y, Pan C, Zhang J, Wang C, *et al*. Glycometabolic reprogramming-induced XRCC1 lactylation confers therapeutic resistance in ALDH1A3-overexpressing glioblastoma. *Cell Metabolism*. 2024; 36: 1696–1710.e10. <https://doi.org/10.1016/j.cmet.2024.07.011>.
- [7] Zhou Z, Yin X, Sun H, Lu J, Li Y, Fan Y, *et al*. PTBP1 Lactylation Promotes Glioma Stem Cell Maintenance through PFKFB4-Driven Glycolysis. *Cancer Research*. 2025; 85: 739–757. <https://doi.org/10.1158/0008-5472.CAN-24-1412>.
- [8] Weinstein JN, Collisson EA, Mills GB, Shaw KRM, Ozenberger BA, Ellrott K, *et al*. The Cancer Genome Atlas Pan-Cancer analysis project. *Nature Genetics*. 2013; 45: 1113–1120. <https://doi.org/10.1038/ng.2764>.
- [9] Zhao Z, Zhang KN, Wang Q, Li G, Zeng F, Zhang Y, *et al*. Chinese Glioma Genome Atlas (CGGA): A Comprehensive Resource with Functional Genomic Data from Chinese Glioma Patients. *Genomics, Proteomics & Bioinformatics*. 2021; 19: 1–12. <https://doi.org/10.1016/j.gpb.2020.10.005>.
- [10] Lee S, Weiss T, Bühler M, Mena J, Lottenbach Z, Wegmann R, *et al*. High-throughput identification of repurposable neuroactive drugs with potent anti-glioblastoma activity. *Nature Medicine*. 2024; 30: 3196–3208. <https://doi.org/10.1038/s41591-024-03224-y>.
- [11] Ren Y, Huang Z, Zhou L, Xiao P, Song J, He P, *et al*. Spatial transcriptomics reveals niche-specific enrichment and vulnerabilities of radial glial stem-like cells in malignant gliomas. *Nature Communications*. 2023; 14: 1028. <https://doi.org/10.1038/s41467-023-36707-6>.
- [12] Stuart T, Satija R. Integrative single-cell analysis. *Nature Reviews Genetics*. 2019; 20: 257–272. <https://doi.org/10.1038/s41576-019-0093-7>.
- [13] Korsunsky I, Millard N, Fan J, Slowikowski K, Zhang F, Wei K, *et al*. Fast, sensitive and accurate integration of single-cell data with Harmony. *Nature Methods*. 2019; 16: 1289–1296. <https://doi.org/10.1038/s41592-019-0619-0>.
- [14] Wan N, Wang N, Yu S, Zhang H, Tang S, Wang D, *et al*. Cyclic immonium ion of lactyllysine reveals widespread lactylation in

- the human proteome. *Nature Methods*. 2022; 19: 854–864. <https://doi.org/10.1038/s41592-022-01523-1>.
- [15] Liu Z, Guo C, Dang Q, Wang L, Liu L, Weng S, *et al.* Integrative analysis from multi-center studies identifies a consensus machine learning-derived lncRNA signature for stage II/III colorectal cancer. *EBioMedicine*. 2022; 75: 103750. <https://doi.org/10.1016/j.ebiom.2021.103750>.
- [16] Oughtred R, Stark C, Breitkreutz BJ, Rust J, Boucher L, Chang C, *et al.* The BioGRID interaction database: 2019 update. *Nucleic Acids Research*. 2019; 47: D529–D541. <https://doi.org/10.1093/nar/gky1079>.
- [17] Ru B, Huang J, Zhang Y, Aldape K, Jiang P. Estimation of cell lineages in tumors from spatial transcriptomics data. *Nature Communications*. 2023; 14: 568. <https://doi.org/10.1038/s41467-023-36062-6>.
- [18] Sharma VK, Singh A, Srivastava SK, Kumar V, Gardi NL, Nalwa A, *et al.* Increased expression of platelet-derived growth factor associated protein-1 is associated with PDGF-B mediated glioma progression. *The International Journal of Biochemistry & Cell Biology*. 2016; 78: 194–205. <https://doi.org/10.1016/j.biocel.2016.07.016>.
- [19] Zhao Z, Zhou Y, Lv P, Zhou T, Liu H, Xie Y, *et al.* NSUN4 mediated RNA 5-methylcytosine promotes the malignant progression of glioma through improving the CDC42 mRNA stabilization. *Cancer Letters*. 2024; 597: 217059. <https://doi.org/10.1016/j.canlet.2024.217059>.
- [20] Wang S, Huang T, Wu Q, Yuan H, Wu X, Yuan F, *et al.* Lactate reprograms glioblastoma immunity through CBX3-regulated histone lactylation. *The Journal of Clinical Investigation*. 2024; 134: e176851. <https://doi.org/10.1172/JCI176851>.
- [21] Barreiro RAS, Guardia GDA, Meliso FM, Lei X, Li WQ, Savio A, *et al.* The paralogues MAGOH and MAGOHB are oncogenic factors in high-grade gliomas and safeguard the splicing of cell division and cell cycle genes. *RNA Biology*. 2023; 20: 311–322. <https://doi.org/10.1080/15476286.2023.2221511>.
- [22] Zhang X, Han J, Fan D, Wang J, Lin X, Zhang H, *et al.* Lysine-40 succinylation of TAGLN2 induces glioma angiogenesis and tumor growth through regulating TMSB4X. *Cancer Gene Therapy*. 2023; 30: 172–181. <https://doi.org/10.1038/s41417-022-00534-6>.
- [23] Ning J, Liu W, Zhang J, Lang Y, Xu S. Ran GTPase induces EMT and enhances invasion in non-small cell lung cancer cells through activation of PI3K-AKT pathway. *Oncology Research*. 2013; 21: 67–72. <https://doi.org/10.3727/096504013X13747716581417>.
- [24] Yuen HF, Chan KK, Grills C, Murray JT, Platt-Higgins A, Eldin OS, *et al.* Ran is a potential therapeutic target for cancer cells with molecular changes associated with activation of the PI3K/AKT/mTORC1 and Ras/MEK/ERK pathways. *Clinical Cancer Research*. 2012; 18: 380–391. <https://doi.org/10.1158/1078-0432.CCR-11-2035>.
- [25] Chen R, Smith-Cohn M, Cohen AL, Colman H. Glioma Subclassifications and Their Clinical Significance. *Neurotherapeutics*. 2017; 14: 284–297. <https://doi.org/10.1007/s13311-017-0519-x>.
- [26] Huse JT, Aldape KD. The evolving role of molecular markers in the diagnosis and management of diffuse glioma. *Clinical Cancer Research*. 2014; 20: 5601–5611. <https://doi.org/10.1158/1078-0432.CCR-14-0831>.
- [27] Gussyatiner O, Hegi ME. Glioma epigenetics: From subclassification to novel treatment options. *Seminars in Cancer Biology*. 2018; 51: 50–58. <https://doi.org/10.1016/j.semcancer.2017.11.010>.
- [28] El-Tanani M, Nsairat H, Mishra V, Mishra Y, Aljabali AAA, Serrano-Aroca A, *et al.* Ran GTPase and Its Importance in Cellular Signaling and Malignant Phenotype. *International Journal of Molecular Sciences*. 2023; 24: 3065. <https://doi.org/10.3390/ijms24043065>.
- [29] Ozugergin I, Piekny A. Complementary functions for the Ran gradient during division. *Small GTPases*. 2021; 12: 177–187. <https://doi.org/10.1080/21541248.2020.1725371>.
- [30] Cao L, She Z, Zhao Y, Cheng C, Li Y, Xu T, *et al.* Inhibition of RAN attenuates influenza A virus replication and nucleoprotein nuclear export. *Emerging Microbes & Infections*. 2024; 13: 2387910. <https://doi.org/10.1080/22221751.2024.2387910>.
- [31] Güttler T, Görlich D. Ran-dependent nuclear export mediators: a structural perspective. *The EMBO Journal*. 2011; 30: 3457–3474. <https://doi.org/10.1038/emboj.2011.287>.
- [32] Yu L, Wei J, Liu P. Attacking the PI3K/AKT/mTOR signaling pathway for targeted therapeutic treatment in human cancer. *Seminars in Cancer Biology*. 2022; 85: 69–94. <https://doi.org/10.1016/j.semcancer.2021.06.019>.
- [33] Ersahin T, Tuncbag N, Cetin-Atalay R. The PI3K/AKT/mTOR interactive pathway. *Molecular BioSystems*. 2015; 11: 1946–1954. <https://doi.org/10.1039/c5mb00101c>.
- [34] Yang Q, Jiang W, Hou P. Emerging role of PI3K/AKT in tumor-related epigenetic regulation. *Seminars in Cancer Biology*. 2019; 59: 112–124. <https://doi.org/10.1016/j.semcancer.2019.04.001>.
- [35] de Visser KE, Joyce JA. The evolving tumor microenvironment: From cancer initiation to metastatic outgrowth. *Cancer Cell*. 2023; 41: 374–403. <https://doi.org/10.1016/j.ccell.2023.02.016>.
- [36] Bikfalvi A, da Costa CA, Avril T, Barnier JV, Bauchet L, Brisson L, *et al.* Challenges in glioblastoma research: focus on the tumor microenvironment. *Trends in Cancer*. 2023; 9: 9–27. <https://doi.org/10.1016/j.trecan.2022.09.005>.
- [37] Du Q, Li R, Wang J, Wang J, Jiang Y, Xu Q, *et al.* RAN potentiates nuclear export of phosphorylated AMPK, reshaping lipid metabolism and impairing immune efficacy in lung adenocarcinoma. *NPJ Precision Oncology*. 2025; 9: 165. <https://doi.org/10.1038/s41698-025-00977-8>.
- [38] Dasso M. The Ran GTPase: theme and variations. *Current Biology*. 2002; 12: R502–R508. [https://doi.org/10.1016/s0960-9822\(02\)00970-3](https://doi.org/10.1016/s0960-9822(02)00970-3).